Scale-resolving simulations of turbulence: Equilibrium boundary layer analysis leading to near-wall closure modeling

Pedram Tazraei[1,*] and Sharath S. Girimaji[1,2,3,†]

[1]*Department of Mechanical Engineering, Texas A&M University, College Station, Texas 77843, USA*
[2]*Department of Aerospace Engineering, Texas A&M University, College Station, Texas 77843, USA*
[3]*Department of Ocean Engineering, Texas A&M University, College Station, Texas 77843, USA*

(Received 14 March 2019; published 23 October 2019)

Equilibrium boundary layer (EBL) analysis is performed on filtered turbulence flow fields for the purpose of deriving key closure models for scale-resolving simulations (SRS) of turbulence. The objective is to convey the near-wall closure modeling advantages of the Reynolds-averaged Navier-Stokes (RANS) method to SRS methodology. In the context of two-equation SRS turbulence closure, the filtered flow field EBL analysis leads to closure models for turbulent transport of unresolved kinetic energy and dissipation as a function of degree of resolution. The resulting model is then employed to perform SRS-PANS (partially averaged Navier-Stokes method) computations of turbulent channel flow. It is first demonstrated that PANS computations yield flow-field statistics that are consistent with filtered-field closure modeling assumptions. The PANS results are then compared against established direct numerical simulation and experimental data. It is exhibited that mean velocity, Reynolds stresses, and qualitative and quantitative coherent-structure features are well captured at a reasonable computational effort.

DOI: 10.1103/PhysRevFluids.4.104607

I. INTRODUCTION

In recent years scale-resolving simulations (SRS) have emerged as a preferred option for computing complex turbulent flows of engineering interest. In order to achieve reasonable results at an affordable computational cost, SRS is envisioned to selectively resolve only vital large-scale turbulence structures on an "accuracy-on-demand" basis. The SRS methods can be broadly classified into two categories: zonal and bridging approaches. In zonal approaches the partitioning of the flow field into high- and low-fidelity parts occurs in physical space. In the regions of the flow with complex coherent structures, the flow field is computed with high-fidelity large-eddy simulations (LES). Other regions of canonical turbulence are computed with Reynolds-averaged Navier-Stokes (RANS) models. Thus, zonal models achieve computational savings due to the use of inexpensive RANS in flow regions of simple turbulence features. The main challenge in the SRS zonal approach is the treatment of the "hand-shake" or "grey" region at the interface of the RANS and LES domains. On the other hand, much like LES, the bridging SRS approach uses the same filtered Navier-Stokes equations throughout the flow domain. The key differences between LES and bridging SRS methods are (i) the bridging SRS methods are intended for resolving a much narrower range of scales than LES; (ii) the SRS filter is implicit and the cut-off length scale is determined by the effective eddy viscosity; and (iii) the SRS closure models solve additional equations for computing the eddy viscosity of the unresolved scales of motion. The SRS effective

*ptazraei@tamu.edu
†girimaji@tamu.edu

cutoff can be varied by suitably modifying the coefficients in the eddy-viscosity model equations in a manner consistent with turbulence physics. The main challenge of the bridging SRS approach is to develop subgrid stress model equations that are suitably sensitive to the implied cut-off length. In principle, bridging SRS computation reduces to RANS in the low-resolution limit and asymptotes to direct numerical simulation (DNS) in the high-resolution limit. In order to accommodate cutoff in larger scales of motion, the bridging SRS subgrid closure model must account for more complex turbulence physics than its LES counterpart.

For computing important statistical features of turbulent boundary layers, the RANS method offers useful advantages over SRS or LES. The SRS and LES approaches are inherently more accurate away from the wall, as they resolve important flow features, but they can be prohibitively expensive for resolving the small scales of motion encountered at the walls. The advantage of RANS at the wall is due to the fact that the closure models are derived from scaling laws established within the equilibrium boundary layer (EBL). There have been many attempts to reduce the LES computational cost at the wall by incorporating features of EBL into subgrid stress models [1–4]. While the resulting "wall-modeled" LES approaches have achieved success, there is opportunity for further improvement of SRS models in the near-wall region.

The focus of this work is on the near-wall modeling for SRS approaches. The bridging SRS approach of choice in this work is the partially averaged Navier-Stokes (PANS) model of Girimaji [5], which has many features in common with the single-point partially integrated transport model (PITM) [6–8]. Multiscale closure of PITM is also discussed in [9]. PANS adapts and extends proven two-equation RANS or second moment closure (SMC) models for representing the effects of subgrid scales on the resolved flow field. The physical rationale and mathematical framework for modifying the RANS model to represent the subgrid physics as a function of scale resolution have been developed in Refs. [5–7,10]. The motivation for using a two-equation closure is that individual evolution equations must be solved for the subgrid velocity and length scales to determine subgrid stress. This approach has already been well documented for a variety of canonical flows [11–13]. The partition between resolved and unresolved fields is defined by specifying the ratios of the unresolved-to-total kinetic energy ($f_k = k_u/k$) and unresolved-to-total specific dissipation rate ($f_\omega = \omega_u/\omega$) [5,14]. The PANS framework for adapting the RANS model developed in [5,10] does not comprehensively address the turbulent transport closure or near-wall behavior. Those works propose a model based solely on scale-interaction arguments. There is a clear and imminent need for advancing the physical fidelity of the SRS transport models.

As mentioned earlier, the RANS turbulent transport models for kinetic energy and dissipation are derived from EBL analysis. This raises the question of whether a similar EBL analysis can be developed for filtered flow fields leading to SRS transport models. The RANS turbulent transport models are expected to reproduce physically consistent one-point statistics only. On the other hand, the SRS approaches are required to yield not only the correct one-point statistical behavior but also emulate important nonlocal and unsteady flow features. Therefore, it is important to ensure that any SRS turbulent transport model produces one-point statistics and key coherent-structure features consistent with the flow physics.

The three key objectives of the current work are:

(1) Adapt and extend equilibrium boundary layer (EBL) analysis to filtered turbulent fields, leading to turbulent transport models for unresolved kinetic energy and unresolved (specific) dissipation.

(2) Perform SRS-PANS simulations of benchmark channel flow and evaluate the PANS behavior in equilibrium log-layer by comparison against DNS statistics of Hoyas and Jiménez [15].

(3) Examine the ability of PANS to capture key qualitative and quantitative aspects of coherent structures in channel flows.

Although much of the closure model development in this paper is in the context of PANS, the analytical framework and closure expressions are applicable to other bridging SRS methods.

The paper is organized as follows. The basic premise of the PANS model, as well as a detailed derivation of the SRS turbulent transport model based on EBL analysis, is described in Sec. II.

Section III discusses the simulated test cases. In Sec. IV, the results of the proposed transport model are assessed by comparing PANS results with DNS data and known features of coherent structures.

II. GOVERNING EQUATIONS

The evolution equations governing an incompressible turbulent flow are continuity and Navier-Stokes equations which are respectively expressed as

$$\frac{\partial V_i}{\partial x_i} = 0, \tag{1}$$

$$\frac{\partial V_i}{\partial t} + V_j \frac{\partial V_i}{\partial x_j} = -\frac{\partial p}{\partial x_i} + \nu \frac{\partial^2 V_i}{\partial x_j \partial x_j}. \tag{2}$$

Here, density is subsumed into the pressure term. A generalized filter is used to decompose the velocity and pressure fields into the resolved and unresolved parts [5]. The filter is taken to be commutative and constant preserving:

$$V_i = U_i + u_i', \quad U_i = \langle V_i \rangle, \ \langle u_i' \rangle \neq 0, \tag{3}$$

$$p = P + p', \quad P = \langle p \rangle, \ \langle p' \rangle \neq 0. \tag{4}$$

where *Vi* is the total velocity and *Ui* is the filtered velocity field. By applying the filter to the Navier-Stokes equations, the momentum equation for the resolved field is given by

$$\frac{\partial U_i}{\partial t} + U_j \frac{\partial U_i}{\partial x_j} = -\frac{\partial \tau(V_i, V_j)}{\partial x_j} - \frac{\partial \langle p \rangle}{\partial x_i} + \nu \frac{\partial^2 U_i}{\partial x_j \partial x_j}. \tag{5}$$

The effect of the unresolved field on resolved velocity-field evolution is manifested *via* the generalized "subfilter stress" $\tau(V_i, V_j)$ [16]. The goal of any bridging SRS model is to develop a suitable closure for the subfilter stress (SFS). The general form of the "subfilter stress" $\tau(V_i, V_j)$ is represented as [16]

$$\tau(V_i, V_j) = \langle V_i V_j \rangle - \langle V_i \rangle \langle V_j \rangle. \tag{6}$$

The PANS bridging SRS approach is based on the premise that RANS-type turbulence closure is well suited for SFS closure, as they were originally developed to represent the physics of the entire spectrum of scales on the mean flow. Accordingly, the original PANS works [5,10] develop the physical foundation and mathematical framework to adapt RANS models for filtered flow fields.

In principle, any RANS closure, including the full Reynolds stress closure model (RSCM) that solves transport equations for all Reynolds stress components, can be adapted to the PANS framework. However, the more sophisticated RANS models will increase the stiffness of the equations and the complexity of the computations. It is therefore important to consider the overall benefits of using higher-level closures. There are two main reasons for employing higher-complexity closure models in the RANS context: (i) anisotropy and nonlinearity of the constitutive relation and (ii) nonlocal effects of turbulence due to history effects and the elliptic nature of pressure. Both these effects are strong functions of wave number. With increasing wave numbers, these effects become less and less significant. In a SRS computation, when the cut-off wave number is high enough to capture any resident coherent structures, (i) much of anisotropy and nonlocality effects are captured in the resolved scales, and (ii) any of these effects residing in the unresolved scales do not significantly affect the main statistics of the flow field. For these reasons, in this work we utilize the simple and robust Boussinesq approximation [5] for the subgrid stress:

$$\tau(V_i, V_j) = \frac{2}{3} k_u \delta_{ij} - 2\nu_u \bar{S}_{ij}, \quad \nu_u = \frac{k_u}{\omega_u}, \quad \omega_u = \frac{\varepsilon_u}{\beta^* k_u}, \tag{7}$$

in which ν_u, S_{ij}, k_u, ε_u, ω_u, and β^* are the unresolved eddy viscosity, strain tensor of the resolved field, unresolved kinetic energy, unresolved dissipation rate, unresolved specific dissipation rate, and closure coefficient, respectively. The goal of PANS closure is to derive suitable evolution equations for the kinetic energy and (specific) dissipation of the unresolved field as a function of the desired resolution. The motivation for a two-equation closure stems from the fact that, at a minimum, unresolved-field length and velocity scales are required to specify SFS with some degree of generality.

The partition between resolved and unresolved scales of motion is characterized in terms of the fractions of unresolved kinetic energy and (specific) dissipation [5]:

$$f_k = \frac{k_u}{k}, \quad f_\varepsilon = \frac{\varepsilon_u}{\varepsilon}, \quad f_\omega = \frac{\omega_u}{\omega} = \frac{f_\varepsilon}{f_k}. \tag{8}$$

Only two of the above three ratios are independent. The two independent parameters determine the effective cut-off length scale of the simulation as a function of the Reynolds number and are called the resolution control parameters. These control parameters prescribe the effective viscosity due to the unresolved scales—the smaller the effective viscosity, more and more scales of the resolved field will be liberated. The relationship between grid size and PANS resolution parameters can be derived using simple scaling arguments [17]:

$$\eta_u > \Delta \rightarrow f_k \geqslant 3\left(\frac{\Delta}{L}\right)^{\frac{2}{3}} \quad \text{where} \quad L = \frac{k^{\frac{3}{2}}}{\varepsilon}, \tag{9}$$

in which η_u is the computational Kolmogorov scale expressed by $[(\nu + \nu_u)^3/\varepsilon_u]^{\frac{1}{4}}$, Δ is the smallest grid dimension, and L is the local turbulence length scale. In high-Reynolds-number flows, it can be reasonably assumed that all of the dissipation is contained in modeled scales, leading to $f_\varepsilon = 1.0$. Thus at high Reynolds numbers, only one parameter (f_k) needs to be specified. For simulating low-Reynolds-number flows, both independent parameters need to be specified. The quantitative criteria for determining optimal f_k value are discussed in Pereira *et al.* [18].

Model equations for the unresolved turbulent kinetic energy (k_u) and specific dissipation rate (ω_u) as functions of resolution control parameters are derived from parent RANS equations using the averaging invariance principle [16] and the fixed point analysis in homogeneous turbulence flows found in Girimaji *et al.* [10]. These equations are given by

$$\frac{\partial k_u}{\partial t} + U_j \frac{\partial k_u}{\partial x_j} = P_u - \beta^* k_u \omega_u + \frac{\partial}{\partial x_j}\left[\left(\nu + \frac{\nu_u}{\sigma_{ku}}\right)\frac{\partial k_u}{\partial x_j}\right], \tag{10}$$

$$\frac{\partial \omega_u}{\partial t} + U_j \frac{\partial \omega_u}{\partial x_j} = \alpha \frac{P_u \omega_u}{k_u} - \alpha\beta^* \omega_u^2 + \alpha\beta^* \frac{\omega_u^2}{f_\omega} - \beta \frac{\omega_u^2}{f_\omega} + \frac{\partial}{\partial x_j}\left[\left(\nu + \frac{\nu_u}{\sigma_{\omega_u}}\right)\frac{\partial \omega_u}{\partial x_j}\right], \tag{11}$$

where the closure coefficients are $\beta^* = 0.09$, $\alpha = 5/9$, and $\beta = 0.075$. The last term on the right-hand side of the above evolution equations represents the transport effects. The turbulent transport closure is not a part of the homogeneous flow fixed point analysis. In the original works [5,10], simple scale-interaction arguments are used to suggest a range of physically permissible unresolved kinetic energy and dissipation Prandtl numbers.

Over the last decade, the PANS methodology has experienced several important developments:

(1) The paradigm that PANS is a DNS of a variable-viscosity medium is developed in Reyes *et al.* [19] to adapt Kolmogorov hypotheses to characterize the unsteady features of the simulated flow field. It is shown that the PANS unsteady field captures important high-order and multipoint statistics of turbulence in accordance with Kolmogorov theory.

(2) A closure model for commutation residual terms is derived in Girimaji and Wallin [20] from the conservation of total energy principle.

(3) The DNS of variable viscosity paradigm is used to derive important criteria for optimal PANS resolution in flows with spatially evolving coherent structures [18].

(4) PANS has been benchmarked against DNS, LES, and experimental data in several canonical flows [11–13,21–23].

(5) A near-wall low-Reynolds-number version of PANS is developed in [23], but it does not address turbulent transport closure.

As mentioned in the Introduction, the objective of the present study is to formally derive and validate the PANS turbulent transport model using EBL analysis.

A. Equilibrium boundary layer analysis for RANS

We first present the RANS-EBL formulation before developing a similar analysis for filtered fields. In the RANS approach, the functional form of the turbulent transport model is presumed from the gradient transport hypothesis, and the closure coefficient (Prandtl number) is derived using equilibrium boundary layer analysis.

The EBL is amenable to the following simplifications:

$$\frac{dk}{dt} = \frac{d\omega}{dt} = 0, \quad \text{and} \quad P = \varepsilon. \tag{12}$$

Further, the following scaling is proposed [24]:

$$k = \frac{u_\tau^2}{\sqrt{c_\mu}}, \quad \tau_{xy} = -u_\tau^2, \quad \text{and} \quad \frac{dU}{dy} = \frac{u_\tau}{\kappa y}, \tag{13}$$

where u_τ and κ are the friction velocity and von Kármán constant, respectively. From the above, the following expressions for production can be derived:

$$P = -\tau_{xy}\frac{\partial U}{\partial y} = \frac{u_\tau^3}{\kappa y}, \tag{14}$$

$$P = \nu_t\left(\frac{\partial U}{\partial y}\right)^2 = \frac{k}{\omega}\frac{u_\tau^2}{\kappa^2 y^2} = \varepsilon. \tag{15}$$

The eddy viscosity can be identified as

$$\nu_t = \frac{k}{\omega} = \kappa u_\tau y. \tag{16}$$

These scalings are employed to determine σ_ω for RANS transport models [24]:

$$\sigma_\omega = \frac{\kappa^2}{\sqrt{\beta^*}}\left(\frac{\beta}{\beta^*} - \alpha\right)^{-1}. \tag{17}$$

There is a wide range of values from 0.384 to 0.41 suggested for the von Kármán coefficient in literature [25]. In the current study, we use $\kappa = 0.41$, which is the standard value employed in open source and commercial codes. After substituting the values of the closure coefficients along with $\kappa = 0.41$ into the expression above, we obtain $\sigma_\omega = 2.0$. This value yields the correct slope of the logarithmic layer in an equilibrium boundary layer. The kinetic energy Prandtl number is set to be equal to σ_ω [24]:

$$\sigma_k = \sigma_\omega\,. \tag{18}$$

B. Equilibrium boundary layer analysis for partially filtered fields

We now seek to develop a similar analysis for PANS equations of filtered fields. For practical applications, variable resolution (VR-PANS), going from RANS at the wall to desired resolution in the wake, is desirable. For VR-PANS, additional modeling of the commutation error residue is needed [20], which will be examined in a future study. Throughout this analysis, we will assume that f_k, f_ε, and f_ω are uniform in space for ease of EBL model derivation. For any decomposition

of resolved and unresolved fields, one can write the following equations for corresponding kinetic energies:

$$\frac{dk_R}{dt} = P_r^m - \varepsilon_r - \gamma_{ru} + T_r, \tag{19}$$

$$\frac{dk_u}{dt} = P_u^m - \varepsilon_u + \gamma_{ru} + T_u, \tag{20}$$

where P_r^m and P_u^m are production of resolved and unresolved kinetic energy due to mean flow, ε_r and ε_u are dissipation occurring in resolved and unresolved fields, γ_{ru} is the spectral transfer of energy from resolved to unresolved fields, and T_r and T_u are the turbulent transport of respective energies.

In order for the boundary layer to be in an equilibrium state, the entire energy spectrum should be in equilibrium. Thus we propose (in a statistical average sense)

$$\frac{dk_R}{dt} \approx \frac{dk_u}{dt} \approx 0, \quad \text{and} \quad T_r = T_u \approx 0. \tag{21}$$

Then it follows that

$$P_r^m - \varepsilon_r - \gamma_{ru} = 0, \tag{22}$$

$$P_u^m - \varepsilon_u + \gamma_{ru} = 0. \tag{23}$$

Further, the overall unresolved kinetic energy production is given by

$$P_u = \gamma_{ru} + P_u^m. \tag{24}$$

That is, the unresolved kinetic energy is generated directly from mean flows as well as for spectral energy transfer from larger scales. These arguments lead to the following:

$$P_u - \varepsilon_u \approx 0. \tag{25}$$

This relationship forms the basis of the filtered EBL analysis. In EBL, we thus suggest the following simplifications to hold true on an average:

$$\frac{dk_u}{dt} = \frac{d\omega_u}{dt} = 0, \quad \text{and} \quad P_u = \varepsilon_u. \tag{26}$$

Let us first consider the unresolved kinetic energy equation. Following the RANS analysis [24], we assume that the molecular viscosity is negligible compared to the eddy viscosity in the EBL. The energy equation is trivially satisfied, confirming that

$$k_u(y) = \text{constant} \tag{27}$$

within the EBL.

Now we consider the unresolved turbulence frequency equation within EBL. Once again, neglecting the effect of molecular transport within EBL leads to

$$0 \approx \alpha \frac{\omega_u P_u}{k_u} - \beta' \omega_u^2 + \frac{\partial}{\partial y}\left(\frac{\nu_u}{\sigma_{\omega u}} \frac{\partial \omega_u}{\partial y}\right). \tag{28}$$

In the equilibrium boundary layer, from the definitions of k_u and ω_u, it follows that

$$k_u = f_k k = f_k \frac{u_\tau^2}{\sqrt{\beta^*}}, \tag{29}$$

$$\omega_u = f_\omega \omega = f_\omega \frac{u_\tau}{\kappa y \sqrt{\beta^*}}, \tag{30}$$

$$\nu_u = \frac{f_k}{f_\omega} \nu_t = \frac{f_k}{f_\omega} u_\tau \kappa y. \tag{31}$$

TABLE I. Details of the test cases examined.

Simulation	Δ_x^+	y_1^+	Δ_z^+	Re_τ	N_y	f_k	$\sigma_{k_u}, \sigma_{\omega_u}$
Case 1	11.25	0.72	5.6	180	50	0.2	0.08
Case 2	34.4	1.7	17.2	550	50	0.1	0.02
Case 3	34.4	0.3	17.2	550	150	0.1	0.02
Case 4	34.4	0.19	17.2	550	200	0.1	0.02
Case 5	34.4	1.7	17.2	550	50	0.15	0.045
Case 6	34.4	1.7	17.2	550	50	0.2	0.08
Case 7	23	1.7	17.2	550	50	0.1	0.02
Case 8	34.4	0.19	17.2	550	200	0.1	2.0 (Unmodified)
Case 9	59	0.53	19	950	120	0.1	0.02
DNS1[a]	9		6.7	186	97		
DNS2[a]	13		6.7	547	257		
DNS3[a]	11		5.7	934	385		

[a]From Ref. [15].

After substituting for k_u and ω_u from the scalings defined in Eqs. (29) and (30) into the evolution equation of the modeled specific dissipation rate, Eq. (28), the following relationship between the modified specific dissipation rate $\sigma_{\omega u}$ and other PANS closure coefficients is obtained:

$$\sigma_{\omega u} = \frac{f_k}{f_\omega}\frac{\kappa^2}{\sqrt{\beta^*}}\left(\frac{\beta}{\beta^*} - \alpha\right)^{-1}. \tag{32}$$

Comparison of Eq. (32) with the RANS counterpart, Eq. (17), leads to the following Prandtl number for unresolved turbulence frequency:

$$\sigma_{\omega u} = \frac{f_k}{f_\omega}\sigma_\omega. \tag{33}$$

We propose that the kinetic energy Prandtl numbers maintain the same ratio as the RANS counterpart. This leads to

$$\sigma_{ku} = \frac{f_k}{f_\omega}\sigma_k, \tag{34}$$

where σ_k and σ_ω are the RANS Prandtl numbers.

The Prandtl number for unresolved kinetic energy and dissipation obtained above from the EBL analysis is consistent with the zero-transport model (ZTM) proposed in [10]. The ZTM model is obtained when the resolved scales transport of unresolved kinetic energy or dissipation is negligible. In the remainder of the paper we perform PANS simulations to verify and validate the proposed transport model in the turbulent channel flow.

III. SIMULATION PROCEDURE

We perform the benchmark turbulent channel flow PANS simulations using the incompressible finite volume solver in OpenFOAM [26]. Table I summarizes different computational and physical resolutions of the conducted PANS simulations. The DNS of Hoyas and Jiménez [15] serves as the reference for the purpose of validation study.

A computational domain of dimensions $4h \times 2h \times 2h$ respectively in the streamwise, wall-normal, and spanwise directions has been considered, where h is the channel half-height. Hexahedral meshes with uniform streamwise and spanwise grid resolutions and stretched wall-normal spacing have been generated. All the grid resolutions reported in Table I are in viscous wall units.

Flow through the channel is sustained by prescribing a constant pressure gradient in the streamwise direction for three different friction Reynolds numbers of $u_\tau\, h/\nu = 180$, 550, and 950. A cyclic boundary condition is applied in the streamwise and spanwise directions, and a no-slip condition is employed at the top and bottom walls. All of the statistics reported here are obtained by temporal averaging over $50h/u_\tau$ time units and spatial averaging in homogeneous directions.

The discretization in space and time is of second order, and the number of subiterations is dictated by the requirement that the residuals at each time step should not exceed 10^{-6}. In addition, in order to ensure the stability of the time integration, the maximum local Courant number is set to a conservative value, $CFL < 0.6$.

IV. RESULTS AND DISCUSSION

The results are presented in three parts. In the first part we ensure that the key modeling assumptions are upheld in the computed results. Next, we demonstrate that the PANS single-point statistics in the EBL compare well against DNS data. Finally, the PANS vorticity structures are examined for qualitative and quantitative consistency against established experimental results.

A. Internal consistency

The principal function of any subgrid model is to simulate the correct level of eddy viscosity and ensure the overall energy level is captured. For the PANS approach to serve as a reasonable SRS scheme, it is very important to ensure that the simulation produces (i) the prescribed degree of viscosity reduction and (ii) the correct kinetic energy balance. We will first examine if PANS simulations produce the desired behavior. In this section, we verify that PANS computed results are consistent with the prescribed parameters and modeling assumptions.

Consider a PANS simulation with prescribed f_k and f_ε or f_ω. We define the viscosity reduction factor (f_ν) as the ratio between PANS viscosity value and that of the total fluctuations or RANS under similar conditions:

$$f_\nu \equiv \frac{\nu_u}{\nu_t}. \tag{35}$$

The expected or prescribed value of the ratio is

$$(f_\nu)_{\text{prescribed}} = \frac{f_k^2}{f_\varepsilon} = \frac{f_k}{f_\omega}. \tag{36}$$

It is reasonable to demand that, on average, the computed results are consistent with the prescribed eddy-viscosity ratio.

For the case of channel flow, the average subgrid PANS viscosity is a function of the wall-normal distance and can be computed as follows:

$$\nu_u(y) = \overline{(k_u/\omega_u)}(y). \tag{37}$$

The viscosity of the total field is estimated from the computations using the total kinetic energy and total dissipation:

$$\nu_t(PANS) = c_\mu \frac{k_t^2}{\varepsilon_t} = c_\mu \frac{\left(\overline{k_u} + k_r\right)^2}{\left(\overline{\varepsilon_u} + \varepsilon_r\right)}, \tag{38}$$

where k_r, ε_u, and ε_r are obtained as follows from the PANS computation:

$$k_r(y) = \overline{V_i V_i} - \bar{V}_i \bar{V}_i, \tag{39}$$

$$\varepsilon_u = \beta k_u \omega_u, \quad \text{and} \quad \varepsilon_r = 2\nu[\overline{S_{ij}S_{ij}} - \bar{S}_{ij}\bar{S}_{ij}]. \tag{40}$$

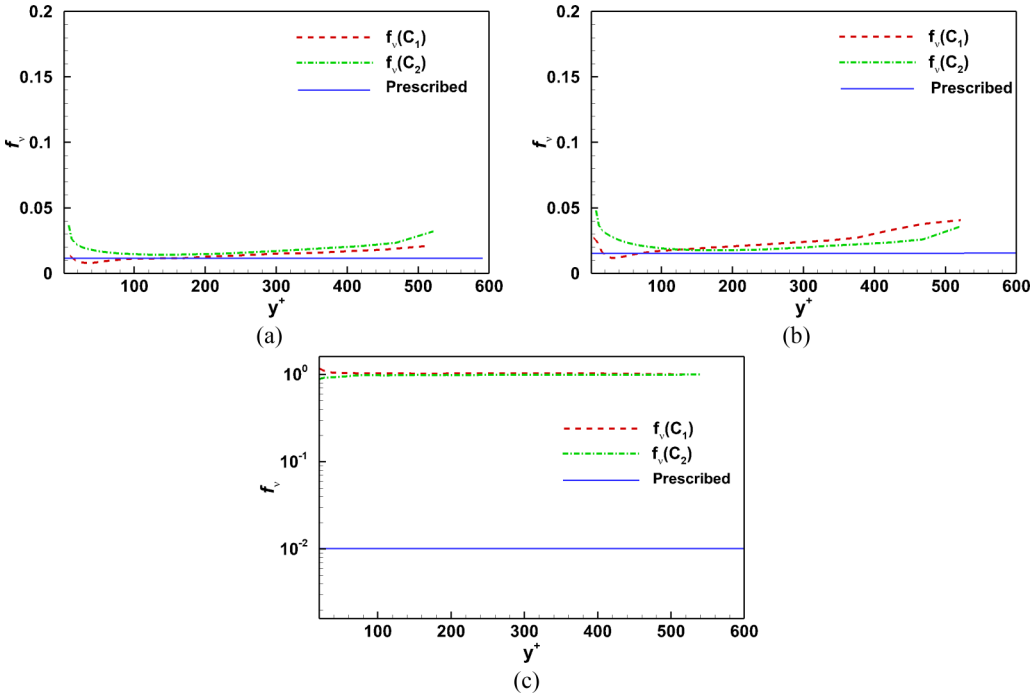

FIG. 1. Consistency profiles for $\mathrm{Re}_\tau = 550$: (a) case 2, (b) case 5, and (c) case 8.

A second approach to estimating the total viscosity is to perform a RANS simulation for the same flow conditions. Based on these two estimates of total viscosity, we define two metrics for computed eddy-viscosity ratio:

$$(f_\nu)_{C1} = \frac{\nu_u(\mathrm{PANS})}{\nu_t(\mathrm{PANS})}, \tag{41}$$

and

$$(f_\nu)_{C2} = \frac{\nu_u(\mathrm{PANS})}{\nu_t(\mathrm{RANS})}. \tag{42}$$

First we verify the consistency between the two estimates of the computed eddy-viscosity ratio and the prescribed ratio for the case of $\mathrm{Re}_\tau = 550$. We also include results from PANS calculation (case 8) in which the turbulent transport is not modified according to the EBL analysis. As shown in Table I, the PANS transport coefficients in case 8 are retained at the RANS values. Figure 1(a) shows the comparison between prescribed and computed values for case 2 ($f_k = 0.1$) in which the PANS transport coefficient is modified according to the EBL analysis. Clearly both C1 and C2 computed eddy-viscosity estimates are in good agreement with prescribed value of 0.01. In Fig. 1(b) a similar comparison is made for case 5 ($f_k = 0.15$) in which the transport coefficients are also modified. Again, the agreement between computed and prescribed ratios is good. Next, we compare case 8 ($f_k = 0.1$) in which the transport coefficients are unmodified from RANS values [Fig. 1(c)]. The computed eddy-viscosity ratio is close to unity rather than the prescribed value of $f_\nu = 0.01$. This clearly demonstrates the importance of modifying the transport coefficient in accordance with EBL analysis. Unless the transport coefficients are modified, the PANS eddy-viscosity value approaches that of RANS irrespective of f_k values specified. It will be shown later that the flow structures computed in case 8 (Unmodified coefficients) do not display a large range of resolved scales.

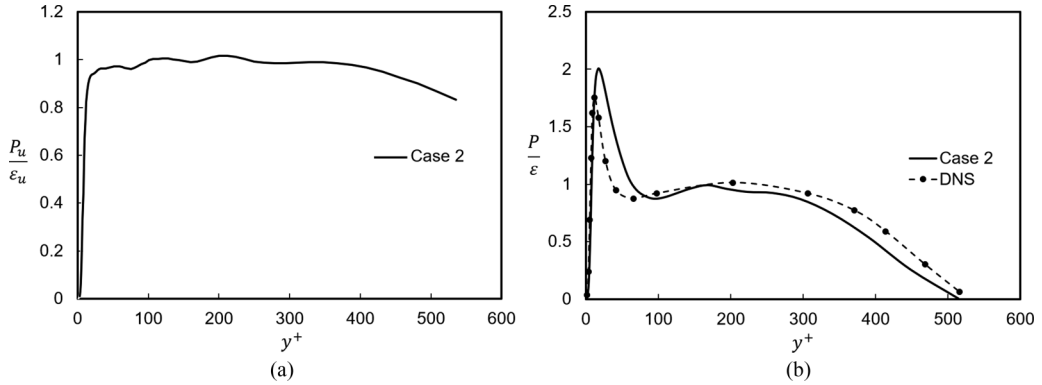

FIG. 2. Production-to-dissipation ratio for $\mathrm{Re}_\tau = 550$ in terms of budgets of (a) subgrid kinetic energy and (b) total kinetic energy.

Having established that the PANS simulation (with modified coefficients) does indeed produce the required reduction in eddy viscosity, we next investigate if the correct balance between production and dissipation is attained. Toward this end, we examine two important ratios: production-dissipation ratio of the unresolved field (P_u/ε_u) and total field (P_t/ε_t). The various production terms are obtained as follows:

$$P_u = 2\nu_u \overline{S_{ij} S_{ij}} \quad \text{and} \quad P_t = -\overline{u_i' u_j'} \overline{\frac{\partial V_i}{\partial x_j}}. \tag{43}$$

It is important to note that due to the unsteady nature of P_u and ε_u, they have been averaged over homogeneous planes as a function of wall distance. The two important ratios as a function of wall-normal distance is shown in Fig. 2(a). There is a clear balance between unresolved production and unresolved dissipation of energy within the logarithmic layer, which effectively decouples the buffer layer and wake flow regions as dictated by physics. Comparison of total production-to-dissipation ratio obtained from the same PANS simulation is now compared against the DNS data of Hoyas and Jiménez [15]. Apart from the region very close to the wall, the agreement is quite reasonable.

We have established that the PANS model produces the prescribed degree of viscosity reduction and reasonable production-dissipation balance. Now we proceed to the validation stage where the PANS statistics and flow structures are compared against established data.

B. One-point statistics

1. Mean flow field

The grid convergence study in terms of the mean velocity field is shown in Fig. 3(a). Cases 2, 3, and 4 in Table I examine the grid convergence in the wall-normal direction, while cases 2 and 7 assess the grid convergence in the stream parallel direction. For the cases with modified coefficients, all three grids considered ($N_y = 50, 150, 200$) converge to the DNS data. The case with unmodified coefficient (case 8), however, exhibits a significant deviation, even with the highest resolution studied ($N_y = 200$). This finding once again emphasizes the importance of turbulent transport coefficients.

Figure 3(b) exhibits the PANS mean velocity profiles at three different Re_τ values: 180, 550, and 950. The results show that the right slope of the log layer is recovered at all Reynolds numbers.

In Fig. 3(c), the mean profiles obtained for three different f_k values are shown for the case of $\mathrm{Re}_\tau = 550$. All these simulations are run on the coarsest grid resolution, with only 204 000 grid cells. As expected, by decreasing the f_k value, a higher amount of unsteadiness within the flow field is resolved, and the PANS results converge to the DNS profile.

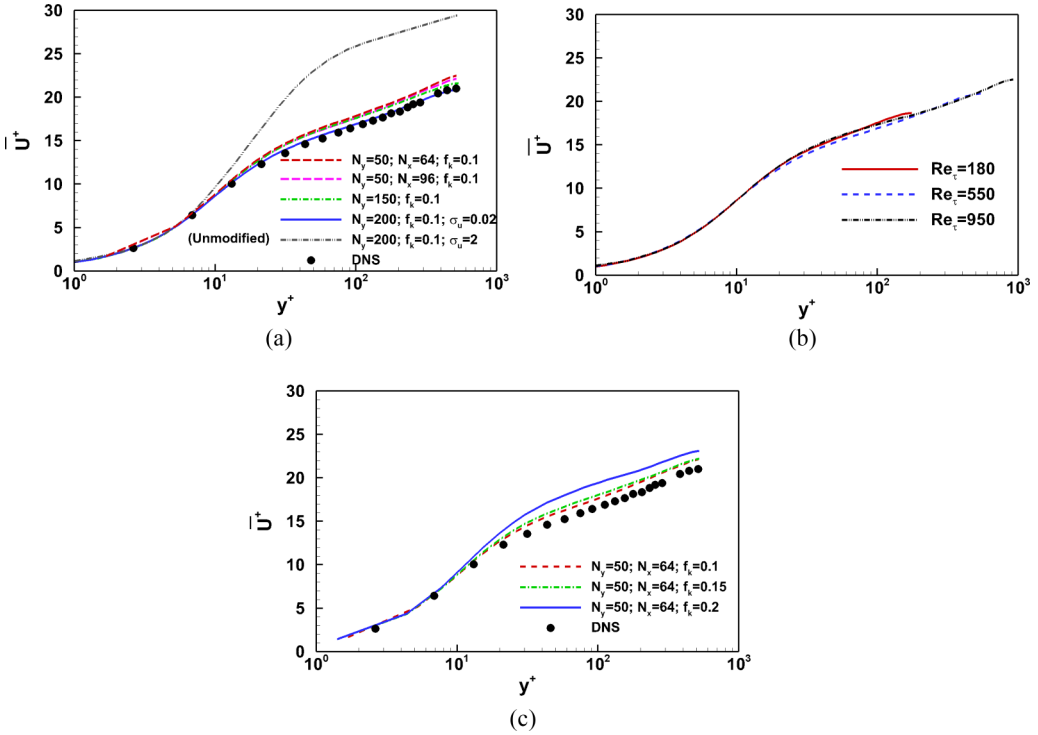

FIG. 3. Mean velocity profiles for different simulation parameters: (a) grid size N_y, (b) Re_τ, (c) and f_k values. DNS data are taken from Hoyas and Jiménez [15].

2. Reynolds stresses

Figure 4 displays the Reynolds shear stress and anisotropy profiles for $f_k = 0.1$ and $R_\tau = 550$ at different grid resolutions. For all resolutions considered, the PANS shear stress is in excellent agreement with the DNS data. The anisotropy of PANS Reynolds stresses is exhibited on the invariant map [27], shown in Fig. 4(b). All cases shown exhibit the correct degree of anisotropy as a function of wall distance. The anisotropy starts at the two-component limit near the wall and proceeds toward the one-component state. Finally, it evolves along the axisymmetric expansion line, approaching isotropic state near the centerline.

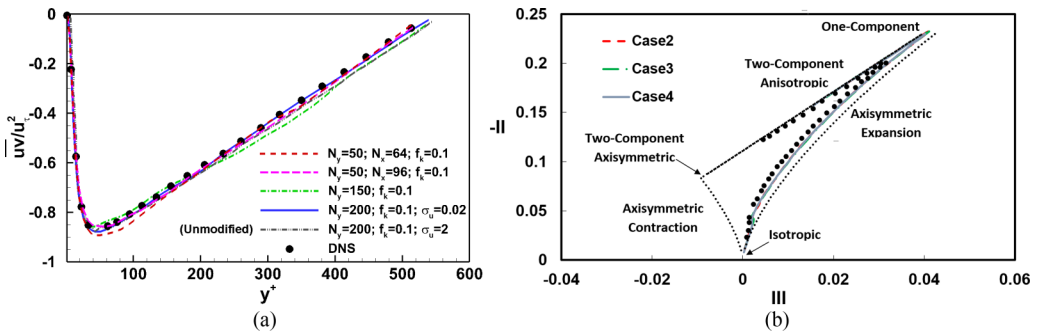

FIG. 4. Reynolds stresses at different grid resolutions for $\mathrm{Re}_\tau = 550$: (a) shear stress profile and (b) anisotropy profile on invariant map.

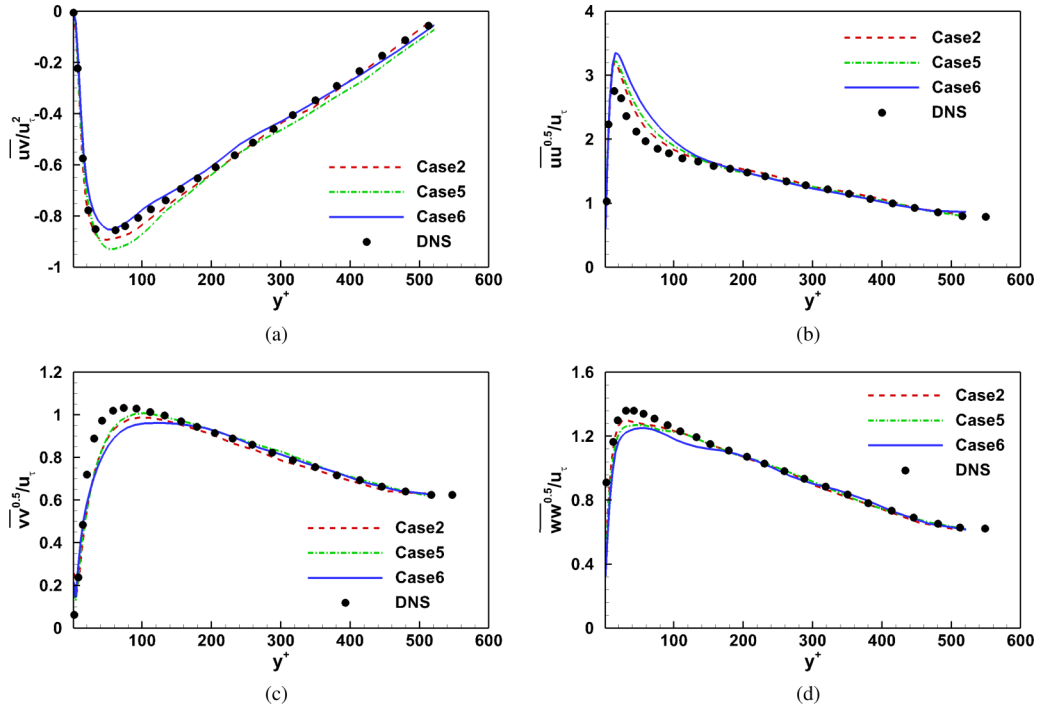

FIG. 5. Reynolds stresses as a function of physical resolution (f_k) for $\mathrm{Re}_\tau = 550$: (a) shear stress, (b) normal streamwise stress, (c) wall-normal stress, and (d) normal spanwise stress.

The f_k dependence of the different Reynolds stress components is shown in Fig. 5. Once again, the PANS results converge to DNS values with decreasing f_k. For the case of $f_k = 0.1$, the agreement is quite good.

C. Multipoint statistics and structures

1. Energy spectra

To demonstrate the scale-resolving capability of WR-PANS, plots of power spectral density of streamwise velocity fluctuations corresponding to case 4 in Table I are shown in Fig. 6. In order to obtain the temporal energy spectra, a large number of samples are recorded at three different wall-normal locations: $y^+ = 50$, 100, and 150. The spectrum is normalized by the local turbulent

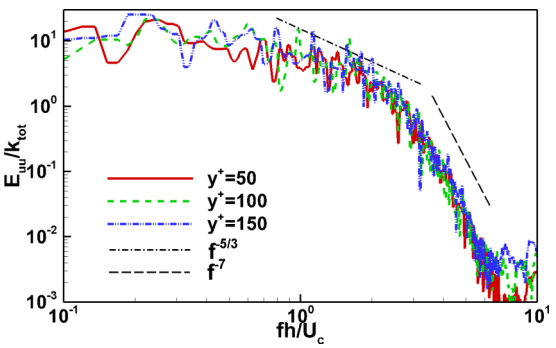

FIG. 6. One-dimensional frequency spectra of streamwise velocity at three wall distances in case 4.

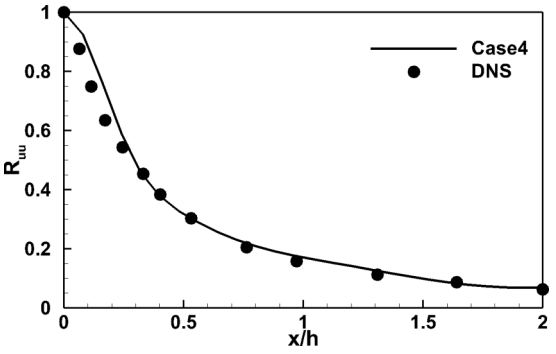

FIG. 7. Two-point correlations R_{uu} in the streamwise direction at $y^+ = 330$. Solid circles are DNS of Sillero *et al.* [30].

kinetic energy, and frequency is scaled by the centerline velocity U_c and channel half-height (h). In addition, to improve the signal clarity, a Hanning window [28] was applied to obtain the spectra. Figure 6 illustrates the computed spectra at the three locations. Each spectrum exhibits a $-5/3$ slope at the large-scale side of the inertial range. Then at smaller inertial scales, the spectrum exhibits a -7 slope. The slopes of the spectra agree very well with the spectral behavior of the boundary layer shown in Wu and Moin [29]. Thus, PANS simulation results yield the correct spectral scaling.

2. Two-point correlation

To further demonstrate the ability of PANS to capture turbulence structures, we now examine the spatial two-point correlations in case 4 (Fig. 7). The PANS two-point streamwise velocity correlation function is compared against the DNS data of Sillero *et al.* [30]. The agreement is reasonable for small separation distances and excellent for larger separations. The discrepancy at small separation distances is to be expected as PANS uses a closure model for representing small-scale physics. The larger scales are captured more accurately, leading to better agreement of the two-point correlations at larger separation distances.

3. Coherent structures

In evaluating SRS methods, it is very important to look beyond low-order statistics and examine unsteady features and flow structures. Our goal here is to establish that PANS computations capture

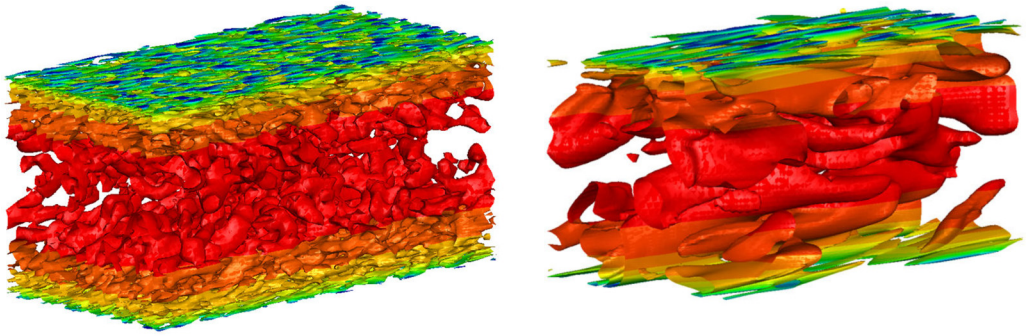

(a) (b)

FIG. 8. Assessment of the modified transport coefficients in terms of turbulence structures for $\mathrm{Re}_\tau = 550$: (a) case 4 and (b) case 8.

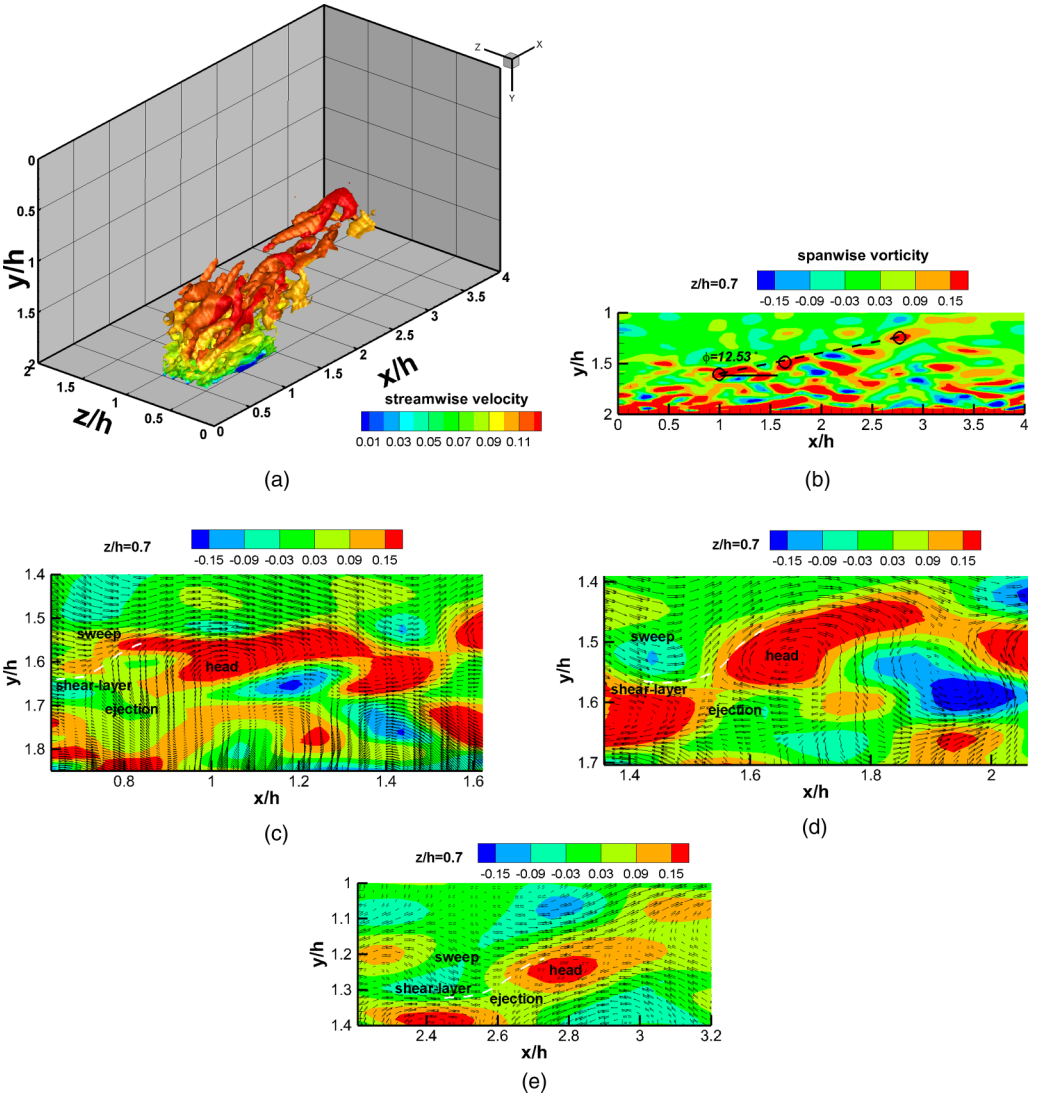

FIG. 9. Organization of turbulence structures for $Re_\tau = 550$. (a) λ_2 isosurfaces colored by streamwise velocity, (b) hairpin packet in spanwise vorticity contour: (c) first hairpin, (d) second hairpin, and (e) third hairpin.

key vorticity features characteristic of boundary layers. For the purpose of vortex visualization, λ_2 isosurfaces representing the minimum local pressure have been employed [31].

Figure 8 illustrates λ_2 isosurfaces, colored by the local streamwise velocity, for cases 4 and 8. The difference between PANS simulations with modified transport coefficients (case 4) and unmodified coefficients (case 8) is immediately evident. The reduced eddy viscosity in the modified case leads to the liberation of a broader range of unsteady scale (case 4). On the other hand, the unmodified case (case 8) exhibits very few unsteady scales. This finding is consistent with the viscosity ratio exhibited in Fig. 1. Thus, the modified model leads to a prescribed degree of viscosity reduction and captures a wider range of scales. Next, we will establish that the unsteady scales exhibit correct physical behavior.

While cases 2–4 show adequate resolution for capturing one-point statistics, for scrutinizing the details of small-scale vorticity structures we use the highly resolved case 4 in Fig. 9. Figure 9(a) provides a three-dimensional illustration of the λ_2 isosurfaces, colored by the local streamwise velocity. For a more quantitative examination, we also present the vorticity contours on a streamwise-wall-normal plane in Fig. 9(b). From these figures we can identify different sets of organized motions referred to as "coherent structures." These structures mostly take the form of a hairpin, which is consistent with the observations of Theodorsen [32].

Figure 9(a) shows resolved hairpin structures of different forms: symmetric, asymmetric, or cane shape. Three distinguishable hairpins, along with some partially formed ones, are observed in the figure shown. Since the spanwise component of velocity is nonzero, one-legged hairpins are most prominent. This figure also shows that the grouped hairpins are aligned in a ramplike shape in the streamwise direction at an angle $\phi = 12.5^\circ$. This value of streamwise alignment angle lies in the range of $12^\circ < \phi < 20^\circ$ established by Christensen and Adrian [33] for fully developed wall-bounded turbulent flows in this Reynolds number range.

Next we focus on a single packet to examine the flow-structure organization using "quadrant analysis" [34]. Figures 9(c)–9(e) capture ejection and sweep mechanisms on the x-y plane of $z/h = 0.7$, going through the head of hairpins in the packet. By following fluctuation velocity field vectors, this plot depicts how the low-speed near-wall fluid ejects away from the wall and the high-speed outer layer fluid sweeps toward the wall. The shear layer at which low- and high-momentum fluids meet is also clearly visible. The head of the hairpins, often referred to as the signature of coherent structures, which corresponds to a strong spanwise vorticity region, is also clearly evident. It should be emphasized that case 7 (with unmodified coefficients) does not capture any of the flow structures at the same degree of computational resolution.

Overall, PANS, with transport equations modified according to EBL analysis, captures the channel flow statistics and flow structures adequately at reasonable computational expense.

V. CONCLUSION

The objective of this study is to derive turbulent transport models for two-equation closures in the context of scale-resolving simulations (SRS) of turbulence. Toward this end, along the lines of RANS methodology, we develop the equilibrium boundary layer analysis of filtered flow fields. The analysis leads to a closure model for turbulent transport Prandtl numbers $\sigma_{\omega u}$ and, ultimately, to σ_{ku}, in terms of resolution control parameters f_k, f_ω.

Employing the new turbulent transport closure models, PANS simulations of turbulent channel flow are performed at different Reynolds numbers. It is first demonstrated that PANS computations do yield the prescribed eddy-viscosity reduction. Further, the computations exhibit the required balance between production and dissipation. Then the PANS results are compared against established DNS and experimental data. The mean flow profile, Reynolds stress magnitude, and anisotropy are well captured by the PANS computations. Analyses of the energy spectra and two-point correlation further confirm the fidelity of PANS methodology. Finally, it is also shown that unsteady flow structures such as hairpin packets are simulated adequately.

The analysis and simulations presented in this paper represent an important step forward toward using two-equation closures for scale-resolving simulations of practical turbulent flows. The development in this work focuses on constant f_k resolution. Work is currently underway to extend the model for spatially varying f_k. This will enable PANS simulation to go from RANS ($f_k = 1$) at the wall to high degrees of resolution ($f_k < 1$) in the interior of the flow.

ACKNOWLEDGMENT

The authors acknowledge support provided by the Texas A&M Division of Research, High Performance Research Computing.

[1] U. Piomelli and E. Balaras, Wall-layer models for large-eddy simulations, Annu. Rev. Fluid Mech. **34**, 349 (2002).
[2] S. Kawai and J. Larsson, Wall-modeling in large eddy simulation: Length scales, grid resolution, and accuracy, Phys. Fluids **24**, 015105 (2012).
[3] S. T. Bose and G. I. Park, Wall-modeled large-eddy simulation for complex turbulent flows, Annu. Rev. Fluid Mech. **50**, 535 (2018).
[4] M. Wang and P. Moin, Dynamic wall modeling for large-eddy simulation of complex turbulent flows, Phys. Fluids **14**, 2043 (2002).
[5] S. S. Girimaji, Partially averaged Navier–Stokes model for turbulence: A Reynolds-averaged Navier–Stokes to direct numerical simulation bridging method, J. Appl. Mech. **73**, 413 (2006).
[6] R. Schiestel and A. Dejoan, Towards a new partially integrated transport model for coarse grid and unsteady turbulent flow simulations, Theor. Comput. Fluid Dyn. **18**, 443 (2005).
[7] B. Chaouat and R. Schiestel, A new partially integrated transport model for subgrid-scale stresses and dissipation rate for turbulent developing flows, Phys. Fluids (1994–present) **17**, 065106 (2005).
[8] B. Chaouat, The state of the art of hybrid RANS/LES modeling for the simulation of turbulent flows, Flow, Turbul. Combust. **99**, 279 (2017).
[9] B. Chaouat and R. Schiestel, From single-scale turbulence models to multiple-scale and subgrid-scale models by fourier transform, Theor. Comput. Fluid Dyn. **21**, 201 (2007).
[10] S. S. Girimaji, E. Jeong, and R. Srinivasan, Partially averaged Navier–Stokes method for turbulence: Fixed point analysis and comparison with unsteady partially averaged Navier–Stokes, J. Appl. Mech. **73**, 422 (2006).
[11] S. Lakshmipathy and S. S. Girimaji, Partially averaged Navier–Stokes (PANS) method for turbulence simulations: Flow past a circular cylinder, J. Fluids Eng. **132**, 121202 (2010).
[12] E. Jeong and S. S. Girimaji, Partially averaged Navier–Stokes (PANS) method for turbulence simulations flow past a square cylinder, J. Fluids Eng. **132**, 121203 (2010).
[13] P. Razi, P. Tazraei, and S. Girimaji, Partially averaged Navier–Stokes (PANS) simulations of flow separation over smooth curved surfaces, Int. J. Heat Fluid Flow **66**, 157 (2017).
[14] S. Lakshmipathy and S. Girimaji, Partially-Averaged Navier-Stokes method for turbulent flows: k-w model implementation, in *44th AIAA Aerospace Sciences Meeting and Exhibit, 9–12 January 2006, Reno, Nevada* (AIAA, Reston, VA, 2006), AIAA Paper 2006-119.
[15] S. Hoyas and J. Jiménez, Reynolds number effects on the Reynolds-stress budgets in turbulent channels, Phys. Fluids (1994–present) **20**, 101511 (2008).
[16] M. Germano, Turbulence: The filtering approach, J. Fluid Mech. **238**, 325 (1992).
[17] S. S. Girimaji and K. S. Abdol-Hamid, Partially-averaged Navier Stokes model for turbulence: Implementation and validation, in *43rd AIAA Aerospace Sciences Meeting and Exhibit, 10–13 January 2005, Reno, Nevada* (AIAA, Reston, VA, 2005), AIAA Paper 2005-502.
[18] F. S. Pereira, L. Eça, G. Vaz, and S. S. Girimaji, Challenges in scale-resolving simulations of turbulent wake flows with coherent structures, J. Comput. Phys. **363**, 98 (2018).
[19] D. A. Reyes, J. M. Cooper, and S. S. Girimaji, Characterizing velocity fluctuations in partially resolved turbulence simulations, Phys. Fluids (1994–present) **26**, 085106 (2014).
[20] S. S. Girimaji and S. Wallin, Closure modeling in bridging regions of variable-resolution (VR) turbulence computations, J. Turbul. **14**, 72 (2013).
[21] F. Pereira, G. Vaz, L. Eça, and S. Girimaji, Simulation of the flow around a circular cylinder at Re = 3900 with partially averaged Navier–Stokes equations, Int. J. Heat Fluid Flow **69**, 234 (2018).
[22] P. Ranjan and A. Dewan, Partially averaged Navier–Stokes simulation of turbulent heat transfer from a square cylinder, Int. J. Heat Mass Transfer **89**, 251 (2015).
[23] B. Basara, S. Krajnovic, S. Girimaji, and Z. Pavlovic, Near-wall formulation of the partially averaged Navier–Stokes turbulence model, AIAA J. **49**, 2627 (2011).
[24] D. C. Wilcox, *Turbulence Modeling for CFD* (DCW Industries, La Canada, CA, 1998), Vol. 2.
[25] K. A. Chauhan, H. M. Nagib, and P. A. Monkewitz, Evidence on non-universality of Karman constant, in *Progress in Turbulence II* (Springer, New York, 2007), pp. 159–163.

[26] H. Jasak, A. Jemcov, and Z. Tukovic, OpenFOAM: A C++ library for complex physics simulations, in *Proceedings of the International Workshop on Coupled Methods in Numerical Dynamics, Dubrovnik, Croatia, 1000, 1* (University, Faculty of Mechanical Engineering and Naval Architecture, 2007), pp. 1–20.

[27] J. L. Lumley and G. R. Newman, The return to isotropy of homogeneous turbulence, J. Fluid Mech. **82**, 161 (1977).

[28] W. H. Press, S. A. Teukolsky, W. T. Vetterling, and B. P. Flannery, Numerical Recipes in C++, *The Art of Scientific Computing* (Cambridge University Press, Cambridge, England, 1992), Vol. 2, p. 1002.

[29] X. Wu and P. Moin, Direct numerical simulation of turbulence in a nominally zero-pressure-gradient flat-plate boundary layer, J. Fluid Mech. **630**, 5 (2009).

[30] J. A. Sillero, J. Jiménez, and R. D. Moser, Two-point statistics for turbulent boundary layers and channels at Reynolds numbers up to $\delta^+ \approx 2000$, Phys. Fluids **26**, 105109 (2014).

[31] J. Jeong and F. Hussain, On the identification of a vortex, J. Fluid Mech. **285**, 69 (1995).

[32] T. Theodorsen, The structure of turbulence, in *50 Jahre Grenzschichtforschung*, edited by H. Görtler and W. Tollmien (Vieweg+Teubner Verlag, Wiesbaden, 1955), pp. 55–62.

[33] K. Christensen and R. J. Adrian, Statistical evidence of hairpin vortex packets in wall turbulence, J. Fluid Mech. **431**, 433 (2001).

[34] W. Willmarth and S. Lu, Structure of the Reynolds stress near the wall, J. Fluid Mech. **55**, 65 (1972).